

Lateral viscosity variations beneath Antarctica and their implications on regional rebound motions and seismotectonics

Georg Kaufmann^{a,*}, Patrick Wu^b, Erik R. Ivins^c

^a *Institut für Geophysik, Universität Göttingen, Herzberger Landstr. 180, 37075 Göttingen, Germany*

^b *Department of Geology and Geophysics, University of Calgary, Calgary, Alberta, Canada T2N 1N4*

^c *MS 300-233 Jet Propulsion Laboratory, California Institute of Technology, 4800 Oak Grove Drive, Pasadena, CA 91109-8099, USA*

Received 5 March 2004; accepted 4 August 2004

Abstract

The Antarctic Ice Sheet has experienced large ice volume changes during the late Pleistocene glacial cycles. However, the exact amount and areas of mass change are difficult to establish, as both glaciological reconstructions and climate models rely on relatively sparse data sets, when compared to Northern Hemisphere data. We assess the potential contributions to present-day crustal motions and seismicity from glacially-induced ice mass changes. Three different scenarios for the late-Pleistocene ice-sheet distributions are considered. The viscoelastic response of the bedrock is computed for two earth models, a model with radially varying mantle viscosity only, and a model with three-dimensional viscosity variations based on a recent seismic tomographical study. In the latter model, East Antarctica is underlain by a stiff cratonic root, while the upper mantle underneath West Antarctica is weak.

Our predicted present-day crustal motions depend strongly on the ice model chosen, with vertical motions focused on areas of former late Pleistocene ice domes. The horizontal motions are greatly affected by the earth rheology, as the horizontal flow pattern is controlled by the flow from the stiff East Antarctic cratonic root to the weaker West Antarctic mantle. Glacially-induced changes in fault stability margin are positive over much of Antarctica, indicating a seismically quiet state due to the large present-day ice sheet. At the site of the 1998 Balleny Island Earthquake ($M_w = 8.1$), the stresses are relatively small by comparison, and interestingly become more prone to stress failure, when a three-dimensional earth model is assumed.

© 2004 Elsevier Ltd. All rights reserved.

Keywords: Antarctic Ice Sheet; Glacial isostatic adjustment; Present-day motions; Faulting

* Corresponding author. Tel.: +49 551 397462; fax: +49 551 397459.

E-mail address: gkaufman@uni-geophys.gwdg.de (G. Kaufmann).

1. Introduction

The reconstruction of the Antarctic Ice Sheet throughout the last glacial cycles is one of the major goals of Antarctic glaciologists. Indirect observations such as successions of ancient beaches recording relative sea-level changes are rare in Antarctica. Of special importance is the evolution of the marine-based West-Antarctic Ice Sheet (WAIS), which may be very sensitive to changes in climate. Our understanding of the past, present, and future dynamics of this large ice sheet is critical for assessing the role of Antarctica in future climate change scenarios. Improvements in measuring geodetic signatures reflecting the isostatic response to fluctuations in ice volume may play a prominent role in further constraining the general environmental setting of the contemporary Antarctic Ice Sheet. Here, continuous Global Positioning System (GPS) monitoring of the present-day motions and the measurement of secular changes in gravity have been proposed as an important supplementary information for ice sheet reconstructions (James and Ivins, 1995, 1997, 1998; Zwartz et al., 1999; Tregoning et al., 2000; Wahr and Davis, 2002).

Currently, ice models for the last glacial cycle in Antarctica are either derivatives of the CLIMAP model (Denton and Hughes, 1981), such as the ANT3 (Nakada and Lambeck, 1988), ICE-3G (Tushingham and Peltier, 1991), and ICE-4G models (Peltier, 1994), or more recent revisions such as the D91 model (Denton et al., 1991) and the ANT5 and ANT6 models (Nakada et al., 2000). In general, the predicted postglacial signal of crustal uplift for the CLIMAP-based models is large, with uplift above 10 mm/year over West Antarctica and less than 5 mm/year over East Antarctica (James and Ivins, 1998). Peak values are around 20–25 mm/year over the Ross and Ronne-Filchner Ice Shelves and the Antarctic Peninsula (for localities refer to Fig. 1). The D91 and ANT6 models result in less uplift, as the ice mass loss during the last deglaciation has been substantially reduced. Still, areas such as the Antarctic Peninsula and the Ross Ice Shelf are predicted to rise by about 6–15 mm/year. However, the timing of deglaciation has been shown to be a key parameter controlling the crustal motion signal.

One of the more intriguing aspects of the Antarctic crust revolves around its apparent muted seismicity level, this in light of ice unloading comparable in size to late-Pleistocene glacial changes in Scandinavia. Numerical models for glacial retreat from LGM in Scandinavia, eastern Canada and the Wilkes Basin in Antarctica (Wu et al., 1999; Wu and Johnston, 2000; Ivins et al., 2003) all predict the promotion of brittle failure stresses well in excess of those thought to drive aftershocks in interplate shear zones (King and Cocco, 2001). Why then are relatively few earthquakes recorded in the interior of the continent? Might the crust there experience heightened levels of seismicity just after deglaciation followed by reduced seismicity thereafter, as suggested by Behrendt (1999)?

Recent data obtained from the installation of temporary broadband seismometers and new permanent stations indicate, however, that there is significant seismic activity in the 2–4 Ms magnitude range (Bannister and Kennett, 2002; Reading, 2002; Studinger et al., 2003). During the next decade in Antarctica the refinement of glacial load history, the increased frequency of seismic array deployments, and the duration of GPS-based crustal motion studies, may allow the crust there to be used as a regional laboratory for better understanding the relationship between loading–unloading and brittle failure.

Antarctica maintains one of the largest and most dramatic topographic and geologic discontinuities found within continental interiors: the Transantarctic Mountain Range Front (TAMRF). Seismic tomography indicates that this crustal discontinuity extends deep within the mantle (Danesi and Morelli, 2001; Ritzwoller et al., 2001) and this paper undertakes a first step toward explicitly accounting for the implied

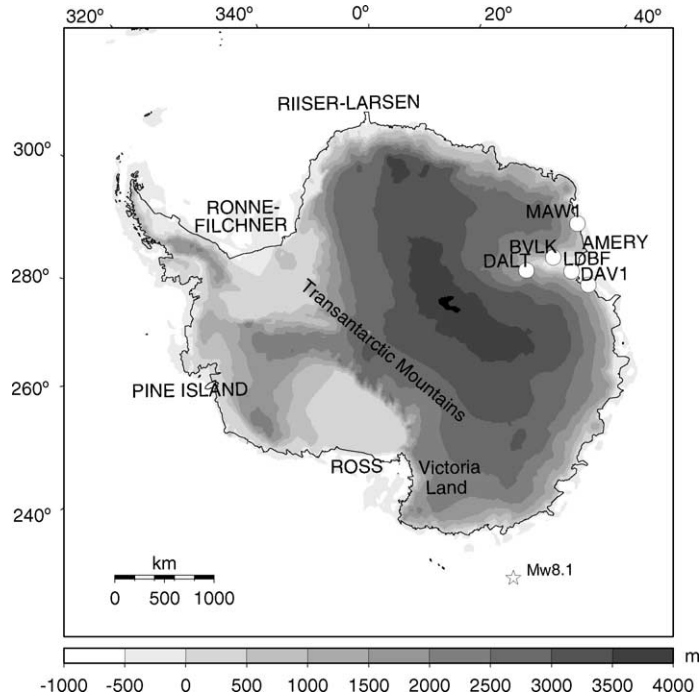


Fig. 1. Topography of Antarctica. Shown are also permanent GPS stations in the Lambert Glacier region (circles). The diamond marks the epicenter of the 1998 Balleny Island ($M_w = 8.1$) earthquake.

rheological variations in predictions of both rebound present-day crustal motions and failure stresses. Some of the differences found in the three-dimensional (3D) models, in contrast to 1D approximations, are dramatic.

The glacial isostatic adjustment of the earth as a result of mass redistributions during the ice-age cycles is successfully modelled within the framework of global glacial isostatic adjustment theory (Peltier, 1974; Farrell and Clark, 1976; Mitrovica et al., 1994a; Milne and Mitrovica, 1998). However, while the complex three-dimensional variation of the combined ice and water load is fully taken into account (Mitrovica et al., 1994b; Peltier, 1996; Lambeck et al., 1998), the properties of the earth's crust and mantle are assumed to vary in the radial direction only. This latter assumption, which simplifies the modelling procedure significantly, ignores the complex three-dimensional structure of the earth's interior as seen by seismic tomographical imaging (Danesi and Morelli, 2001; Ritzwoller et al., 2001; Su and Dziewonski, 1991; Li and Romanowicz, 1996; Trompert, 1998; Ekström and Dziewonski, 1998). Several studies have been carried out in the past to infer the effects of lateral variations in mantle properties on observations related to the glacial isostatic adjustment process. These studies indicate that the effects of lateral variations in viscosity can significantly affect motions induced by glacial isostasy. While most of these studies, based on simple axisymmetrical ice load histories, were intended to assess the effects of some three-dimensional variations in the earth's mantle in general (Sabadini and Gasperini, 1989; Gasperini and Sabadini, 1989; Kaufmann et al., 1997; Giunchi et al., 1997; Kaufmann and Wu, 1998a; Ni and Wu, 1998; Martinec et al., 2001), studies on more realistic, fully three-dimensional ice and earth models are rare (Kaufmann and Wu, 1998b, 2002b,a; Wu et al., 1998; Kaufmann et al., 2000).

In this paper we investigate the effects of lateral viscosity variations on predictions for present-day motions and stress changes resulting from past ice volume changes in Antarctica. Due to the ambiguity of the glacial history, we employ three drastically different Antarctic ice models for the Late Pleistocene ice-ocean mass imbalance, and focus our attention on the response of the solid earth to the ice-mass changes. Our earth models include realistic, but probably modest lateral variations in viscosity derived from contemporary global seismic tomography and a simple parameterisation of the high-temperature solid-state creep law.

2. Earth models

A layered, isotropic, compressible, Maxwell-viscoelastic half-space with a constant gravitational attraction of $g = 9.82 \text{ m s}^{-2}$ is used to model the glacially-induced perturbations of the solid earth. As shown in other papers in this Special Issue, self-gravitating spherical finite-element earth models have been developed recently to handle lateral and radial heterogeneities in the mantle. However, such models are computationally intensive even with a five degree spatial resolution. Since it has been demonstrated (Wu and Johnston, 1998) that flat earth models work well within the ice margin of loads as large as the Laurentide ice sheet, we continue to employ flat earth models in this study. However, as shown in Wu and Johnston (1998), Wu and van der Wal (2003), the effects of sphericity and self-gravitation become increasingly important as one moves beyond the ice margin. Thus results in this region should be treated with caution and need to be confirmed in future studies, where both sphericity and self-gravitation are taken into account.

We solve the Boussinesq problem for a layered, viscoelastic half-space using the commercial finite-element package Abaqus, which has been modified to include pre-stress in order to allow the deformed free surface to return to its initial equilibrium via viscous flow (Wu, 1992a,b). Thus, the equation that describes the conservation of momentum is given by:

$$\nabla \cdot \sigma - g \nabla (\rho w) = 0, \quad (1)$$

where σ is the incremental stress tensor, ρ the density, g the gravitational acceleration, and w is the vertical displacement. The first term in Eq. (1), the divergence of stress, describes the surface force deforming the earth. The second term arises because the undisturbed earth is assumed to be in hydrostatic equilibrium, with the forces of self-gravitation balanced by the hydrostatic pre-stress. This pre-stress is being advected along with the material when the body deforms either elastically or viscoelastically. Thus, the second term in Eq. (1) represents the gradient of the advected pre-stress, $\rho g w$. The presence of this term is required in order to provide the buoyancy force that is needed to satisfy the boundary conditions in the fluid limit, and without this term, there would be no viscous gravitational relaxation. The validity of the finite-element model to predict glacial isostatic adjustment has been shown previously (Wu and Johnston, 1998).

Earth models consist of a layered viscoelastic lithosphere over a layered viscoelastic mantle. Density ρ , shear modulus μ and bulk modulus κ are volume-averaged values derived from PREM (Dziewonski and Anderson, 1981) (see Table 1 for PREM density and Lamé's parameters). Radial mantle viscosity is fixed to $\eta_{\text{UM}} = 3.6 \times 10^{20} \text{ Pa s}$ in the upper mantle and $\eta_{\text{LM}} = 1.7 \times 10^{22} \text{ Pa s}$ in the lower mantle (Lambeck et al., 1998), the lithospheric thickness is fixed to $h_1 = 100 \text{ km}$. The top 30 km is elastic. Below, the lithosphere is viscoelastic with a viscosity of 10^{24} Pa s . Since most of Antarctica has been

Table 1
Elastic structure of earth models

Depth (km)	λ (Pa)	μ (Pa)	ρ (kg m ⁻³)
0–30	4.6216E+10	3.818E+10	2813
30–100	8.5972E+10	6.749E+10	3378
100–246	8.8966E+10	6.527E+10	3379
246–450	1.1552E+11	7.734E+10	3521
450–550	1.4490E+11	9.904E+10	3818
550–670	1.6792E+11	1.162E+11	3959
670–1220	2.2175E+11	1.804E+11	4543
1220–1800	2.9059E+11	2.153E+11	4862
1800–2320	3.5782E+11	2.466E+11	5148
2320–2886	4.2826E+11	2.775E+11	5420

Based on Dziewonski and Anderson (1981). λ : Lamé's first parameter, μ : shear modulus, $\kappa = \lambda + \frac{2}{3}\mu$: bulk modulus, ρ : density.

subjected to a steadily growing glaciation phase during the last 20–30 million years, the viscoelastic part of the lithosphere has plenty of time to relax.

We compare two sets of earth models: Model 1D represents a laterally homogeneous reference model, with the radial viscosity varying as discussed above (Fig. 2a).

Model 3D includes lateral viscosity variations in the mantle (Fig. 2b–e). The lateral viscosity variations are derived from the spherical earth tomographic model S20A (Ekström and Dziewonski, 1998). The viscosity perturbations in the mantle are obtained by scaling the SH-shear-wave velocity anomalies $d \ln v_s = \delta v_s(r, \theta, \phi)/v_s^0(r)$ from S20A. The spherical coordinates are radius r , latitude θ , and longitude ϕ . Following Ivins and Sammis (1995), we define density and temperature functions as:

$$\begin{aligned}\rho(r, \theta, \phi) &= \rho_0(r) + \delta\rho(r, \theta, \phi), \\ T(r, \theta, \phi) &= T_0(r) + \delta T(r, \theta, \phi),\end{aligned}\quad (2)$$

Here ρ_0 and T_0 are radial reference values, and $\delta\rho$ as well as δT the lateral variations. We assume that lateral density variations depend on temperature variations only, thus with the coefficient of thermal expansion α given we use

$$\delta\rho(r, \theta, \phi) = -\alpha(r)\rho_0(r)\delta T(r, \theta, \phi). \quad (3)$$

The effective viscosity is given by

$$\eta = \frac{\sigma^{1-n}}{A} \exp\left(\frac{E + pV}{RT}\right), \quad (4)$$

with σ the deviatoric stress, n a power-law exponent, A a constant, E the activation energy, p the pressure, V the activation volume, and R the gas constant. We then define the lateral viscosity variation as the ratio of viscosity η to the radially-dependent spherically averaged reference viscosity η_0 :

$$\Delta\eta(r, \theta, \phi) = \frac{\eta(r, \theta, \phi)}{\eta_0(r)}. \quad (5)$$

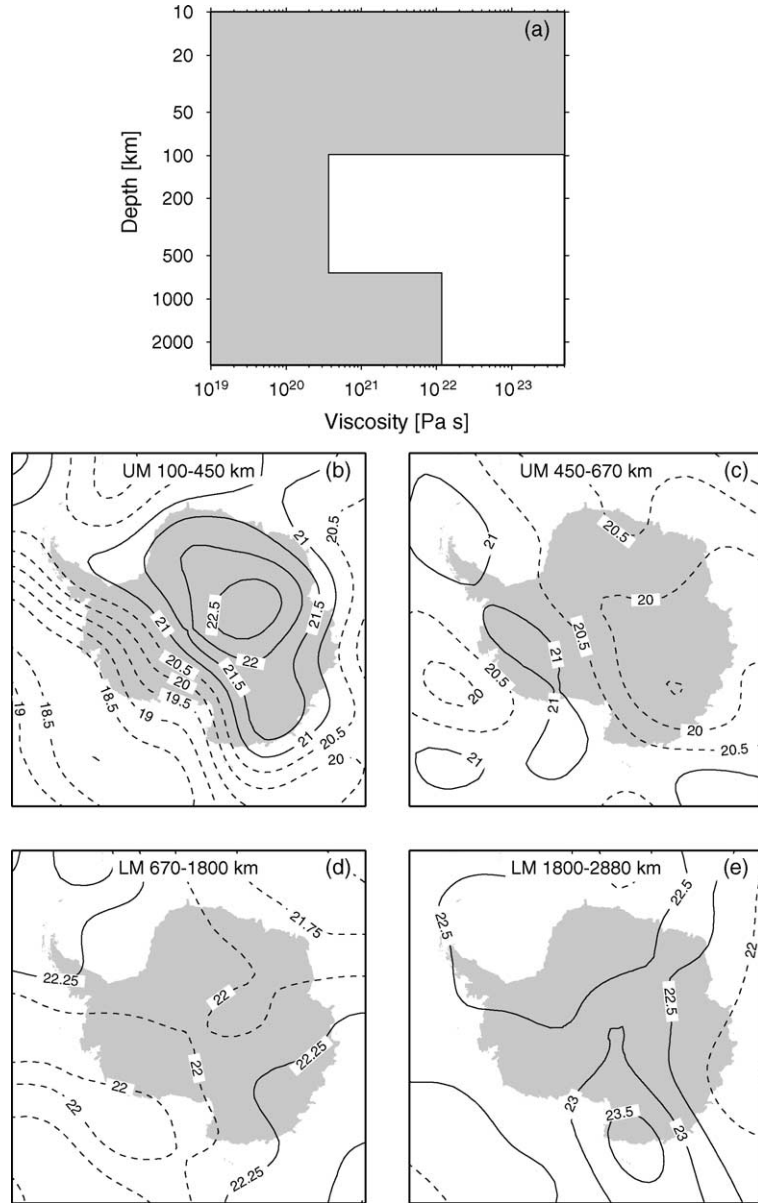


Fig. 2. (a) 1D radial viscosity profile; (b–e) maps of 3D lateral viscosity variations in selected depth intervals. Show is the logarithm of the viscosity, $\log \eta$. Solid lines indicate viscosities above, dashed below the radially-dependent reference viscosity.

Inserting (4) in (5), and assuming $\delta T \ll T_0$ (Ivins and Sammis, 1995), the viscosity ratio is reasonably well approximated as

$$\Delta\eta = \exp\left[\frac{E + pV}{R} \left(-\frac{\delta T}{T_0^2}\right)\right]. \quad (6)$$

Table 2

Depth-dependent parameters for seismic velocity to viscosity conversion

Depth (km)	$(E + pV)/R$ (10^4 K)	α (10^{-5} K $^{-1}$)	T_0 (K) ^a	T_0 (K) ^b
350	8.2	1.725	2088	1990
450	8.3	1.65	2069	2100
550	8.5	1.5	2100	2200
700	8.3	1.463	2300	2230
900	8.7	1.425	2500	2275
1200	9.35	1.3	2600	2296
1500	9.97	1.177	2650	2470
1800	10.6	1.05	2700	2530
2200	11.0	0.9	2675	2562
2600	11.4	0.75	2750	2530
2835	11.7	0.65	3250	2675

From Ivins and Sammis (1995).

^a For layered mantle convection from Tackley et al. (1993).^b For whole mantle convection from Leitch and Yuen (1989).

We can rewrite (3) into

$$\delta T = -\frac{1}{\alpha} \frac{\delta \rho}{\rho_0} = -\frac{1}{\alpha} \frac{d \ln \rho}{d \ln v_s} d \ln v_s. \quad (7)$$

Inserting (7) in (6) then yields

$$\Delta \eta = \exp \left(\frac{E + pV}{R} \frac{1}{\alpha} \frac{1}{T_0^2} \frac{d \ln \rho}{d \ln v_s} d \ln v_s \right). \quad (8)$$

From (8), the lateral viscosity variations are finally derived, based on $d \ln v_s$ as given in S20A, $a = (E + pV)/R$ and α listed in Table 2, and T_0 the temperature profile discussed in Leitch and Yuen (1989) for whole mantle convection or in Tackley et al. (1993) for layered convection (Table 2). Note that both temperature profiles result in similar lateral viscosity variations. In (8), the value of $d \ln \rho / d \ln v_s \simeq 0.3$ is based on high-temperature, high-pressure laboratory experiments (Chopelas and Boehler, 1992; Karato, 1993). The radially-dependent reference viscosity η_0 is fixed to the values introduced above. We thus neglect the possibility that lateral change in chemical composition can also contribute to lateral viscosity variations. Accounting for chemical contrasts could change the lateral contrast in mantle rheology (Klosko et al., 2001). On the other hand, the effect of lateral density contrast has been shown to be insignificant (Wu et al., 1998), thus it will be neglected in this study.

The resulting lateral viscosity variations underneath Antarctica, averaged over depth for four mantle layers, are shown in Fig. 2b–e. In the first mantle layer (100–450 km), the cratonic root underneath East Antarctica is evident, marked by high viscosity values above 10^{22} Pa s. In the next two layers (450–650 and 650–1800 km), lateral viscosity variations are less pronounced. In the lowermost mantle layer (1800–2880 km), a high-viscosity region underneath the Ross Embayment is present, with viscosities up to 10^{24} Pa s.

3. Fault stability margin

For any point in space and time t , we consider the state of stress, described by the normal stress components σ_{ij} , as the superposition of three stress components: (i) a glacially-induced stress σ_{ij}^r , caused by the growth and decay of Late Pleistocene ice sheets; (ii) a tectonic stress S_{ij} ; (iii) and the stress induced by overlying rocks $P_{\text{lith}}\delta_{ij}$. Hence,

$$\sigma_{ij}(t) = \sigma_{ij}^r(t) + S_{ij} + P_{\text{lith}}\delta_{ij}, \quad (9)$$

Note that both the tectonic stress and the stress induced by overlying rocks are assumed to be independent of time, and that we have assumed the lithostatic definition of overburden pressure. We then follow [Wu and Hasegawa \(1996\)](#), and define the fault stability margin FSM as

$$\text{FSM}(t) = \beta[\nu(\sigma_1(t) + \sigma_3(t)) + 2\tau_0] - \frac{1}{2}(\sigma_1(t) - \sigma_3(t)), \quad (10)$$

with $\beta = \sin[\arctan(\nu)]/(2\nu)$ ([Johnston, 1987](#)), σ_1 and σ_3 the maximum and minimum principal stresses, respectively, ν the coefficient of friction, and τ_0 the cohesive strength. From (10), we derive the change in fault stability margin dFSM between two times t and t_0 ,

$$\text{dFSM} = \frac{1}{2}\{[\sigma_1(t_0) - \sigma_3(t_0)] - [\sigma_1(t) - \sigma_3(t)]\} + \nu\beta\{[\sigma_1(t) + \sigma_3(t)] - [\sigma_1(t_0) + \sigma_3(t_0)]\}. \quad (11)$$

Note that (11) is independent of τ_0 . Assuming that the initial stress conditions are close to failure, the condition $\text{dFSM} < 0$ moves faults closer to failure and earthquakes can be triggered, and $\text{dFSM} > 0$ promotes fault stability.

4. Ice models

We have based our model predictions on three Late Pleistocene models for the Antarctic Ice Sheet ([Fig. 3](#)), which we term past ice models. These past ice models are chosen to encompass a wide range of plausible scenarios, both from the total amount of meltwater discharged and the timing of the last deglaciation phase. However, we make no attempt to favour a particular ice model as the most realistic one, as the uncertainty of the last glacial cycle in Antarctica is still too large. The glaciation phase in Antarctica is assumed to be 30 million years long, and all ice models include a present-day Antarctic Ice Sheet based on the model of [Drewry et al. \(1982\)](#). We treat the ice load as linearly increasing to the last glacial maximum, with the longest growth phase at 30 million years in duration. The sensitivity to the assumption of linear growth should be further tested, but is beyond the scope of the present study. A complementary ocean load also varies linearly, corresponding to the eustatic sea-level change based on all ice sheets in the northern and southern hemisphere.

Deglaciation started some 22 ka BP. Model ANT3 ([Nakada and Lambeck, 1988](#)) is based on the CLIMAP reconstruction, it is derived as difference between the last glacial maximum (LGM) Antarctic model from [Denton and Hughes \(1981\)](#) and the present-day Antarctic Ice Sheet of [Drewry \(1982\)](#). Model ANT3 contributes 37 m of eustatic sea-level (ESL) rise since the LGM. The main deglaciation in this model was rather early, with ANT3 melting between 17 and 6.4 ka BP. At the LGM, the model is characterised by three large ice domes, the largest one over the Ronne-Filchner Ice Shelf, and smaller ones over the Ross Ice Shelf and the Antarctic Peninsula, and significant additional ice over the coastal regions in East Antarctica. Model ICE-3G is the Antarctic Ice Sheet reconstruction from the global ice

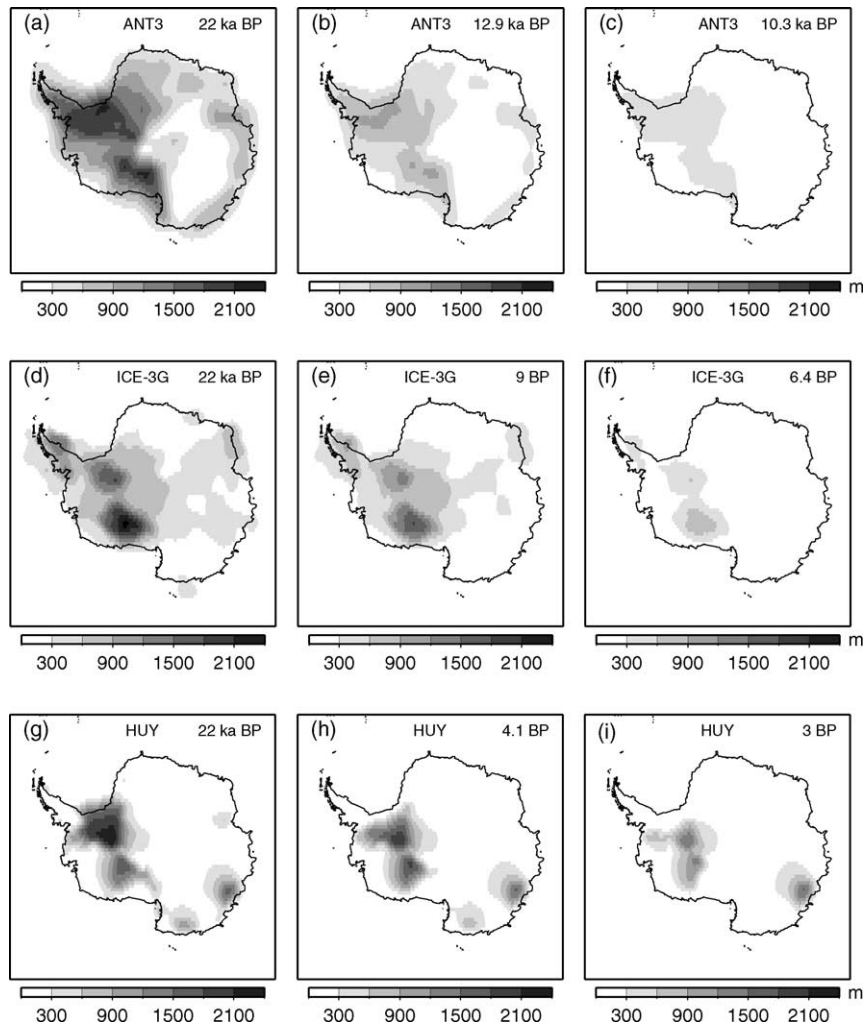


Fig. 3. Deglaciation history for three different ice models: (a–c) ANT3; (d–f) ICE-3G; and (g–i) HUY. Contours are drawn every 300 m. Note that ice heights shown are relative to the present, emphasizing the change in ice thickness. Thus the present-day ice cover is not shown, but models include the present-day ice sheet.

model ICE-3G (Tushingham and Peltier, 1991), it is also based on the CLIMAP reconstruction. The ESL contribution of ICE-3G is 25 m, but the timing of the deglaciation, mainly from 10 to 4 ka BP, favours a late disintegration of the Antarctic Ice Sheet. The disintegration period has been chosen to match sea-level observations in the far field, in this case the Wairau Valley site in New Zealand. At the LGM, this model has the largest ice dome over the Ross Ice Shelf, and two smaller domes over the Ronne-Filchner Ice Shelf and the Antarctic Peninsula. Model HUY from Huybrechts (1990) is derived from thermo-mechanical modelling of ice flow, it contributes only 13 m to ESL. The timing of the deglaciation is in contrast to the two geomorphological models, with melting occurring mostly after 6.4 ka BP and continuing until the present. Between the LGM and around 10 ka BP, the model exhibits ice domes over the Ronne-Filchner and Ross Ice Shelves, and almost no additional ice over East Antarctica, except a small ice dome.

5. Discussion

In the next sections we discuss model predictions of present-day motions and seismicity for the Antarctic region. We compare two different earth models, the radially symmetric 1D viscosity model with a viscosity profile derived by [Lambeck et al. \(1998\)](#), and a three-dimensional viscosity model where the lateral viscosity perturbations are based on a global seismic shear-wave tomography model S20A ([Ekström and Dziewonski, 1998](#)). The uncertainty in ice-sheet history is ameliorated to some degree by using three different ice models. While predictions of present-day motions are calculated for the earth's surface, the change in fault stability margin is derived for a depth of 12.5 km, corresponding to the typical depth of continental and young oceanic intraplate seismicity ([Wiens and Stein, 1983](#); [Maggi et al., 2000](#)).

5.1. Present-day motions

The present-day crustal velocities for the 1D-viscosity model are introduced in [Fig. 4a–c](#), where the vertical components are shown for the three ice models ANT3, ICE-3G, and HUY. For all ice models, we observe rebound of the areas covered by substantial Pleistocene ice masses, as indicated by the positive velocities. Differences in the velocity maps are controlled by two parameters. Firstly, the end of the deglaciation phase correlates to the amount of radial velocity. Ice model ANT3 with its early melting phase ending around 6.4 ka BP results in peak uplift velocities of 7 mm/year. For ice model ICE-3G, where the additional Pleistocene ice cover vanishes around 4 ka BP, peak uplift velocities are twice as large, around 16 mm/year. The pattern of uplift velocity is similar to that of [Fig. 11 of James and Ivins \(1998\)](#), despite the different viscosity profile used. The late-melting ice model HUY experiences a much larger uplift rate, with peak values close to 40 mm/year. Secondly, the centre of uplift for all ice models coincides with the former Pleistocene ice domes. Hence, the extent of Pleistocene ice largely controls the regions, where significant uplift occurs in the models. In [Fig. 4d–f](#), horizontal velocities are shown for the three ice models. As before, the end of the deglaciation phase controls the amplitude of the velocity: peak horizontal values are around 1.5 mm/year (ANT3), 3.5 mm/year (ICE-3G), and 7 mm/year (HUY). The broad pattern is a convergent horizontal flow for all three ice models, and local divergence over the former ice domes of ice models ANT3 and ICE-3G. For ice model HUY, no local divergence is present over the former ice domes. Both vertical and horizontal velocity predictions based on ice model ICE-3G are somewhat comparable to published estimates in [James and Ivins \(1998\)](#), although the latter predictions are based on a stiffer upper mantle viscosity.

Next, we consider present-day velocities resulting from the 3D viscosity model. The vertical velocities are shown in [Fig. 5a–c](#). The general uplift pattern is remarkably similar to the pattern resulting from the 1D viscosity model. The only modification is a slight increase in peak uplift velocity, around 1–2 mm/year more for all ice models. However, the horizontal velocities shown in [Fig. 5d–f](#) are much more affected by the 3D-viscosity structure. Several points can be observed. Firstly, an enhancement of horizontal flow by several mm/year can be seen. Secondly, the flow pattern for the 3D-viscosity model is dominated by a flow direction from East Antarctica to West Antarctica. This is a result of the stiff cratonic root underneath East Antarctica, where horizontal flow is redirected to the weaker, less stiff West Antarctic upper mantle. This large-scale flow pattern completely overprints the local flow around the former ice domes.

Several projects have been set up to monitor crustal motions in Antarctica. In the Lambert Glacier region (feeding the Amery Ice Shelf), [Tregoning et al. \(1999, 2000\)](#) have set up a GPS network in 1998, which now comprises five permanent GPS receivers, two located at the Australian stations Mawson and

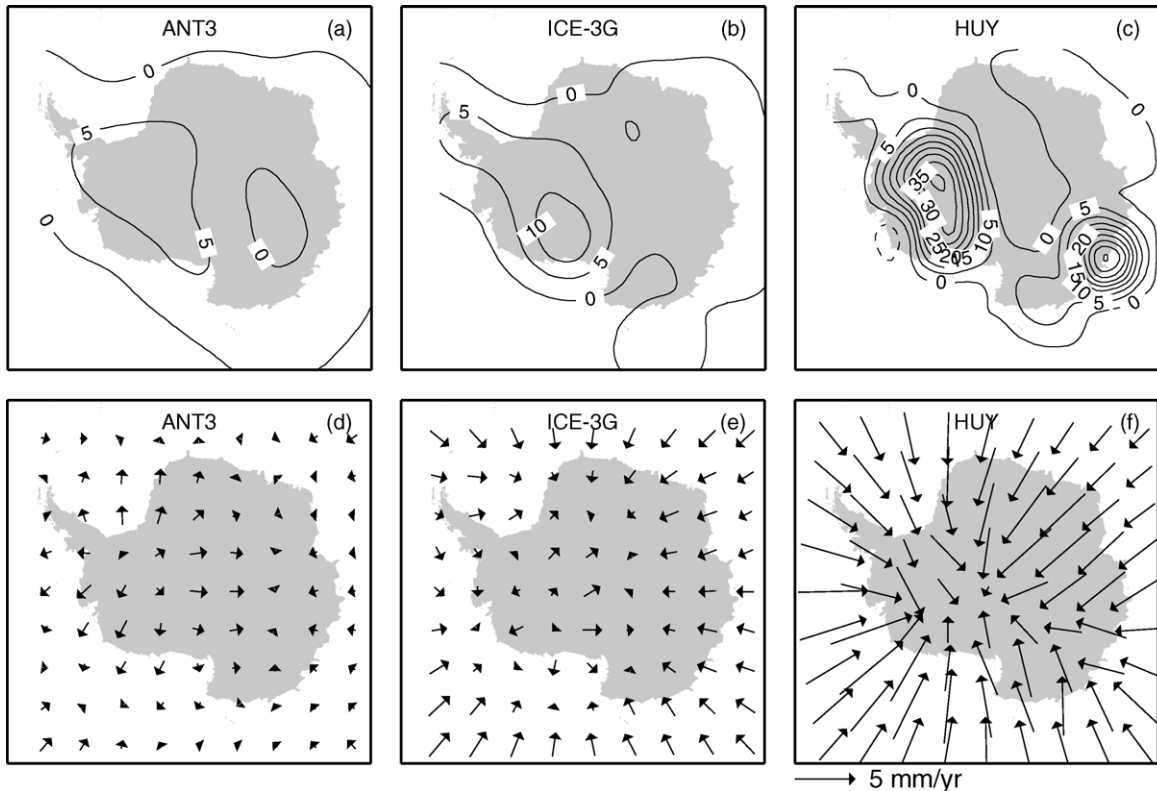


Fig. 4. 1D viscosity: present-day velocities for three different ice models. Positive and negative velocities (in mm/year) are shown as solid and dashed lines, respectively. The scale for the horizontal velocities is given below panel f.

Davis (MAW1 and DAV1), one on the coast at Landing Bluff (LDBF), and the two sites Beaver Lake (BVLK), and Dalton's corner (DALT) further inland (see Fig. 1 for locations). For MAW1, DAV1, and BVLK, reliable GPS-based horizontal velocity estimates are available, and are shown as gray bars in Fig. 6. Also shown in this figure are velocity predictions derived for models 1D viscosity (stars) and 3D viscosity (circles) for the three ice models. We observe a strong southward component induced by glacial isostatic adjustment for all five sites, while eastward velocity predictions are less pronounced. The southward component depends on the ice model, as already discussed above. However, the 3D-viscosity structure induces a significant enhancement of the southward flow for ice models ICE-3G and HUY, while predictions for ice model ANT3 are less affected by the presence of a cratonic root. Eastward velocities are almost unaffected by the cratonic root, which is clear, as the flow pattern induced by the lateral viscosity contrast in the Lambert Glacier Region is directed southward.

5.2. Present-day seismicity

The potential to induce earthquakes by additional glacial stresses due to ice unloading can be seen by plotting the change in fault stability margin, $dFSM$, at present time. This quantity is contoured in Fig. 7. In this figure, an additional tectonic stress component in the direction of the South Pole has been

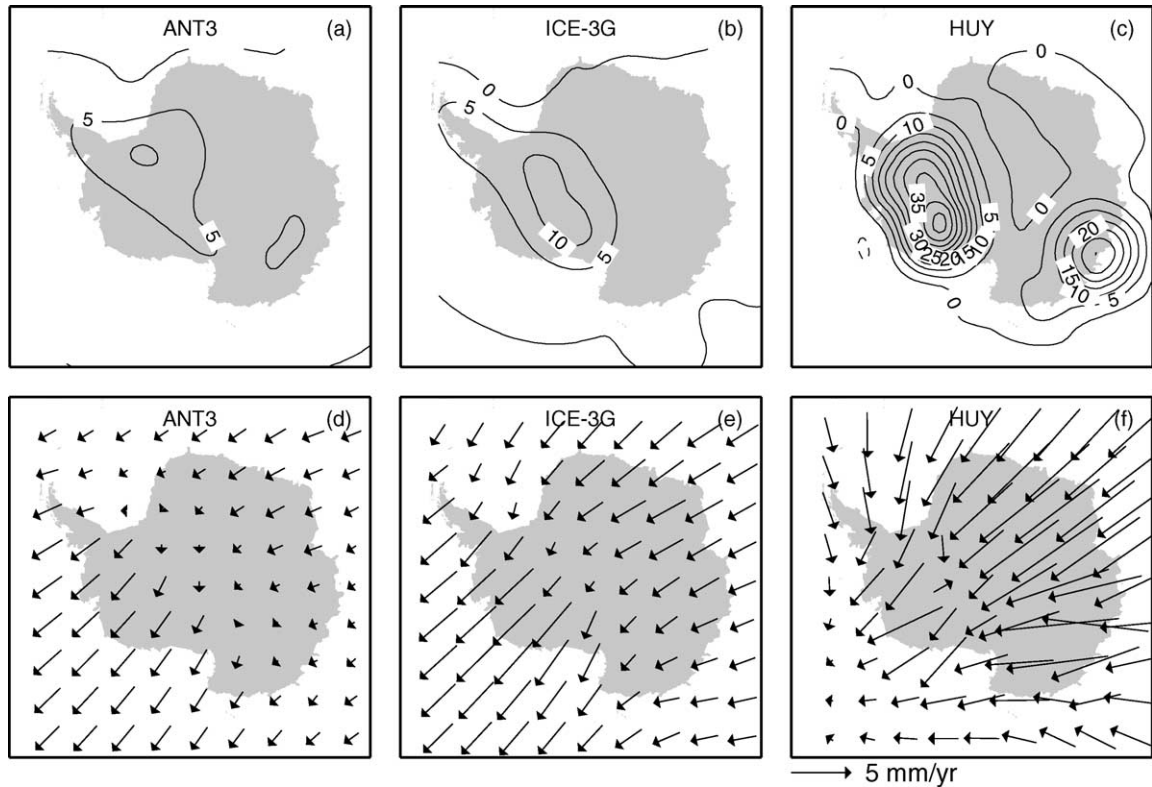


Fig. 5. 3D viscosity: present-day velocities for three different ice models. Positive and negative velocities (in mm/year) are shown as solid and dashed lines, respectively. The scale for the horizontal velocities is given below panel f.

assumed. We argue, that the Antarctic continent is surrounded by oceanic spreading ridges, and generally this spreading is aligned with the continental shelf. Hence, the stress field should reflect this symmetry. In the Victoria Land region, our assumed stress field is roughly in accord with new stress orientation data (for a summary see [Ivins et al., 2003](#)).

In 1998, a large earthquake of magnitude $M_w = 8.1$ occurred 330 km north of the Antarctic Shelf close to Balleny Island ([Fig. 1](#)). This earthquake was a very unusual event, as the quake (epicentre at 300 km depth) occurred around 300 km away from the nearest plate boundary, and stresses do not coincide with surrounding plate boundaries ([Henry et al., 2000](#)). It has been suggested ([Tsuboi et al., 2000](#); [Kreemer and Holt, 2000](#)) that this earthquake might be caused by the ongoing deformation and stress change related to the deglaciation of Antarctica.

For the 1D viscosity model and the three ice models ANT3, ICE-3G, and HUY, dFSM at present is shown in [Fig. 7a–c](#). All ice models predict large positive values for the change in fault stability margin over the former Pleistocene ice domes, with values up to 15 MPa. Hence, fault stability is promoted over Antarctica for all ice models considered, a result of the large normal stress imposed by the present-day ice sheet ([Johnston, 1987](#)). Near the site of the 1998 Balleny Island earthquake, fault stability for the 1D viscosity models is still positive, but much smaller. For the prediction of fault instability at the Balleny Island earthquake site, lithospheric thickness has to be increased substantially ([Ivins et al., 2003](#)).

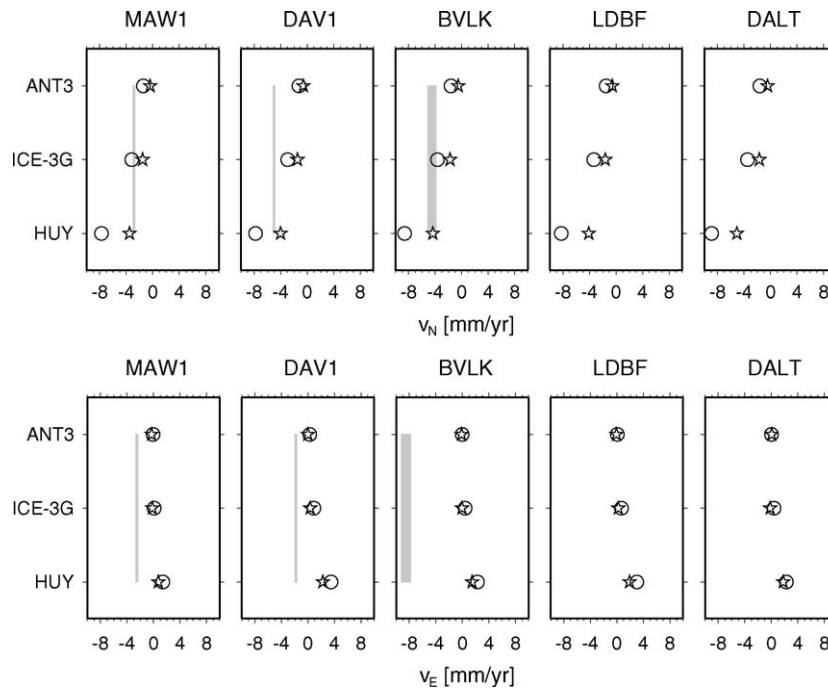


Fig. 6. Predicted horizontal velocities based on changes in the Antarctic Ice Sheet geometry. Predictions are for three ice models, five GPS sites described in the text and two earth models: stars, 1D viscosity; circles, 3D viscosity. Also shown as gray bars are GPS-based velocity estimates based on ITRF96 (MAW1 from bowie.mit.edu/fresh/igsw/series/MAW1_TS.html, DAV1 from bowie.mit.edu/fresh/igsw/series/DAV1_TS.html, BVLK from rse.anu.edu.au/geodynamics/gps/antarctic/daily.gif).

A similar pattern of fracture stress emerges, when we consider the 3D viscosity model for the prediction of dFSM, as shown in Fig. 7d–f. For all three ice models, large positive values for dFSM are predicted for the Antarctic continent. While values for dFSM have even increased over West and East Antarctica, a slight reduction occurred over the TAMRF. More interestingly, the zero contour has moved towards the coast by several hundreds of kilometers, especially around West Antarctica. For all three ice models, the site of the 1998 Balleny Island earthquake is now close to the zero contour, thus enhancing the likelihood of glacially-induced seismicity. This is possibly due to an effective thickening of the lithosphere in East Antarctica. As we have noted before, the 3D viscosity variation modelled is a conservative estimate, larger variations will possibly move the 1998 Balleny Island earthquake site closer to failure.

The choice of ice model significantly influences dFSM, with ICE-3G producing a dFSM closest to failure at the 1998 Balleny Island earthquake site (Fig. 8). This is possibly related to the large additional Pleistocene ice cover close to the Ross Ice Shelf in ICE-3G. For the 1D viscosity model, all ice models predict large positive values for dFSM at the site of the 1998 Balleny Island earthquake. Considering the 3D viscosity model, values for dFSM move closer to zero for all ice models, but the potential to trigger faulting is still small. Another parameter controlling the likelihood of failure is the length of the glaciation phase of the Antarctic Ice Sheet. We have reduced the glaciation phase from 30 to 3 and 1 million years, respectively, testing the hypothesis of a more dynamical Pliocene Antarctic Ice Sheet. As it can be seen from Fig. 8, shorter glaciation phases result in more stable conditions at the Balleny Island earthquake site.

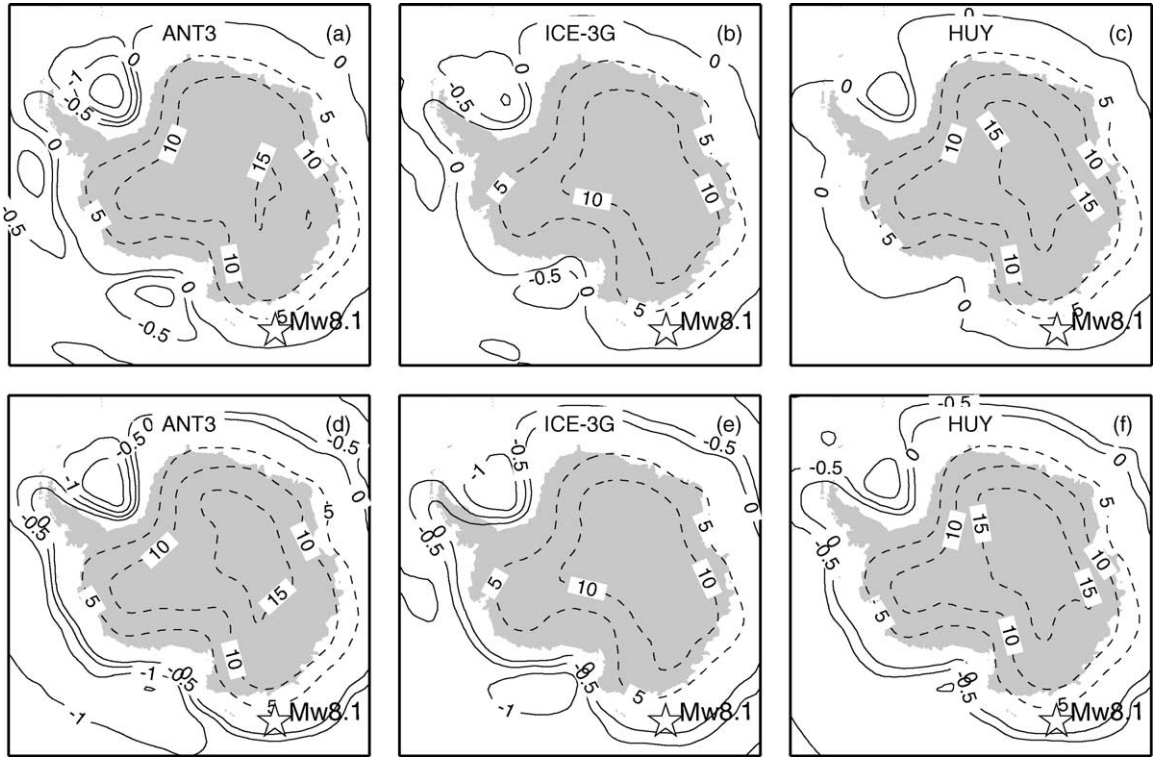


Fig. 7. Change in fault stability margin (in MPa) for three ice models and (a–c) 1D viscosity; (d–f) 3D viscosity. A tectonic background stress perpendicular to spreading ridges (radial) is assumed. Dashed contours give fault stability, while solid contours give fault instability.

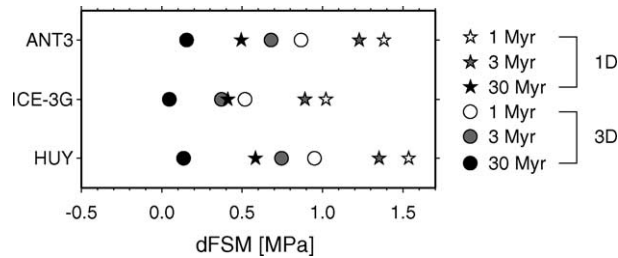


Fig. 8. Fault stability margin at the Balleny Island earthquake location for three different ice models with different glaciation phases and two earth models: stars, 1D viscosity and tectonic stress perpendicular to spreading ridges; circles, 3D viscosity and tectonic stress perpendicular to spreading ridges. Times indicate the length of the glaciation phase.

6. Conclusions

We summarize our numerical results for crustal velocities and fault instability in and around the Antarctic continent, which are driven by variations in Antarctic Ice Sheet geometry through time, with a number of remarks. (i) Uplift is most strongly influenced by the timing of the deglaciation event and the Pleistocene ice sheet distribution, and less sensitive to the viscosity structure. (ii) A cratonic root

induces a strong horizontal flow component from East to West Antarctica, obscuring the original rebound signal. (iii) The large present-day ice cover could suppress seismicity, independent of viscosity structure, provided the long-term load scenario investigated here is realistic. (iv) Fault instability is promoted offshore (e.g. the Balleny Island earthquakes site), if a cratonic root is accounted for. (v) Fault instability is also promoted offshore, if the glaciation phase is sufficiently long.

Acknowledgements

The finite element calculations were performed with the ABAQUS package from Hibbitt, Karlsson and Sorensen Inc. The figures in this paper are drawn using the GMT graphics package (Wessel and Smith, 1991, 1998).

References

- Bannister, S., Kennett, B.L.N., 2002. Seismic activity in the Transantarctic Mountains—results from a broadband array deployment. *Terra Antarctica* 9, 41–46.
- Behrendt, J., 1999. Crustal and lithospheric structure of the West Antarctic Rift System from geophysical investigations—a review. *Global Planet. Change* 23, 25–44.
- Chopelas, A., Boehler, R., 1992. Thermal expansivity in the lower mantle. *Geophys. Res. Lett.* 19, 1983–1986.
- Danesi, S., Morelli, A., 2001. Structure of the upper mantle under the antarctic plate from surface wave tomography. *Geophys. Res. Lett.* 28 (23), 4395–4398.
- Denton, G.H., Hughes, T.J., 1981. *The Last Great Ice Sheets*. John Wiley and Sons, New York.
- Denton, G.H., Prentice, M.L., Burckle, L.H., 1991. Cainozoic history of the Antarctic Ice Sheet. In: Tingey, R.J. (Ed.), *Geology of Antarctica*. Oxford University Press, New York, pp. 365–433.
- Drewry, D.J., 1982. *Antarctica: Glaciological and Geophysical Folio*. Scott Polar Res. Inst., Cambridge.
- Drewry, D.J., Jordan, S.R., Jankowski, E., 1982. Measured properties of the Antarctic Ice Sheet: surface configuration, ice thickness, volume, and bedrock characteristics. *Ann. Glaciol.* 3, 83–91.
- Dziewonski, A.M., Anderson, D.L., 1981. Preliminary reference earth model. *Phys. Earth Planet. Inter.* 25, 297–356.
- Ekström, G., Dziewonski, A.M., 1998. The unique anisotropy of the Pacific upper mantle. *Nature* 394, 168–172.
- Farrell, W.E., Clark, J.A., 1976. On postglacial sea level. *Geophys. J. R. Astr. Soc.* 46, 647–667.
- Gasparini, P., Sabadini, R., 1989. Lateral heterogeneities in mantle viscosity and post-glacial rebound. *Geophys. J.* 98, 413–428.
- Giunchi, C., Spada, G., Sabadini, R., 1997. Lateral viscosity variations and post-glacial rebound: effects on present-day VLBI baseline deformations. *Geophys. Res. Lett.* 24 (1), 13–16.
- Henry, C., Das, S., Woodhouse, J.H., 2000. The March 25, 1988 $M_w = 8.1$ Antarctic Plate earthquake: moment tensor and rupture history. *J. Geophys. Res.* 105, 16097–16119.
- Huybrechts, P., 1990. The Antarctic Ice Sheet during the last glacial–interglacial cycle: a three-dimensional experiment. *Ann. Glaciol.* 14, 115–119.
- Ivins, E.R., James, T.S., Klemann, V., 2003. Glacial isostatic stress shadowing by the Antarctic Ice Sheet. *J. Geophys. Res.* 108 (B12), doi: 10.1029/2002LB002182.
- Ivins, E.R., Sammis, C.G., 1995. On lateral viscosity contrast in the mantle and the rheology of low frequency geodynamics. *Geophys. J. Int.* 123, 305–322.
- James, T.S., Ivins, E.R., 1995. Present-day Antarctic ice mass changes and crustal motion. *Geophys. Res. Lett.* 22 (8), 973–976.
- James, T.S., Ivins, E.R., 1997. Global geodetic signatures of the Antarctic Ice Sheet. *J. Geophys. Res.* 102 (B1), 605–633.
- James, T.S., Ivins, E.R., 1998. Predictions of Antarctic crustal motions driven by present-day ice sheet evolution and by isostatic memory of the Last Glacial Maximum. *J. Geophys. Res.* 103, 4993–5017.
- Johnston, A.C., 1987. Suppression of earthquakes by large continental ice sheets. *Nature* 330, 467–469.

- Karato, S.I., 1993. Importance of anelasticity in the interpretation of seismic tomography. *Geophys. Res. Lett.* 20, 1623–1626.
- Kaufmann, G., Wu, P., 1998. Upper mantle lateral viscosity variations and postglacial rebound: application to the Barents Sea. In: Wu, P. (Ed.), *Dynamics of the Ice Age Earth: A Modern Perspective*. Trans. Tech. Pub., Zürich, Switzerland 583–602.
- Kaufmann, G., Wu, P., 1998. Lateral asthenospheric viscosity variations and postglacial rebound: a case study for the Barents Sea. *Geophys. Res. Lett.* 25 (11), 1963–1966.
- Kaufmann, G., Wu, P., 2002. Glacial isostatic adjustment in Fennoscandia with a three-dimensional viscosity structure as an inverse problem. *Earth Planet. Sci. Lett.* 197 (1–2), 1–10.
- Kaufmann, G., Wu, P., 2002. Glacial isostatic adjustment on a three-dimensional earth: examples from Fennoscandia and the Barents Sea. In: Mitrovica, J.X., Vermeersen, L.L.A. (Eds.), *Ice Sheets, Sea Level and the Dynamic Earth*. AGU Geodyn. Ser. 29, Washington, pp. 293–309.
- Kaufmann, G., Wu, P., Li, G., 2000. Glacial isostatic adjustment in Fennoscandia for a laterally heterogeneous earth. *Geophys. J. Int.* 143 (1), 262–273.
- Kaufmann, G., Wu, P., Wolf, D., 1997. Some effects of lateral heterogeneities in the upper mantle on postglacial land uplift close to continental margins. *Geophys. J. Int.* 128, 175–187.
- King, G., Cocco, M., 2001. Fault interaction by elastic stress changes: new clues from earthquake sequences. *Adv. Geophys.* 44, 1–38.
- Klosko, E.R., Russo, R.M., Okal, E.A., Richardson, W.P., 2001. Evidence for a rheologically strong chemical mantle root beneath the OntongJava Plateau. *Earth Planet. Sci. Lett.* 186, 347–361.
- Kreemer, C., Holt, W.E., 2000. What caused the March 25, 1998 Antarctic plate earthquake?: inferences from regional stress and strain rate fields. *Geophys. Res. Lett.* 27, 2297–2300.
- Lambeck, K., Smither, C., Johnston, P., 1998. Sea-level change, glacial rebound and mantle viscosity for northern Europe. *Geophys. J. Int.* 134, 102–144.
- Leitch, A.M., Yuen, D.A., 1989. Internal heating and thermal constraints on the mantle. *Geophys. Res. Lett.* 16, 1407–1410.
- Li, X.D., Romanowicz, B., 1996. Global mantle shear velocity model developed using nonlinear asymptotic coupling theory. *J. Geophys. Res.* 101 (B10), 22245–22272.
- Maggi, A., Jackson, J.A., McKenzie, D., Priestley, K., 2000. Earthquake focal depths, effective elastic thickness, and the strength of the continental lithosphere. *Geology* 28, 495–498.
- Martinec, Z., Čadež, O., Fleitout, L., 2001. Can the 1D viscosity profiles inferred from postglacial rebound data be affected by lateral changes in the lithospheric thickness?. *Geophys. Res. Lett.* 28 (23), 4403–4406.
- Milne, G.A., Mitrovica, J.X., 1998. Postglacial sea-level change on a rotating earth. *Geophys. J. Int.* 133, 1–19.
- Mitrovica, J.X., Davis, J.L., Shapiro, I.I., 1994. A spectral formalism for computing three-dimensional deformations due to surface loads 1. Theory. *J. Geophys. Res.* 99 (B4), 7057–7073.
- Mitrovica, J.X., Davis, J.L., Shapiro, I.I., 1994. A spectral formalism for computing three-dimensional deformations due to surface loads 2. Present-day glacial isostatic adjustment. *J. Geophys. Res.* 99 (B4), 7075–7101.
- Nakada, M., Kimura, R., Okuno, J., Moriwaki, K., Miura, H., Maemoku, H., 2000. Late Pleistocene and Holocene melting history of the Antarctic Ice Sheet derived from sea-level variations. *Mar. Geol.* 167, 85–103.
- Nakada, M., Lambeck, K., 1988. The melting history of the late Pleistocene Antarctic Ice Sheet. *Nature* 333, 36–40.
- Ni, Z., Wu, P., 1998. Effects of removing concentric positioning on postglacial vertical displacement in the presence of lateral variation in lithospheric thickness. *Geophys. Res. Lett.* 25 (16), 3209–3212.
- Peltier, W.R., 1974. The impulse response of a Maxwell Earth. *Rev. Geophys. Space Sci.* 12 (4), 649–669.
- Peltier, W.R., 1994. Ice age paleotopography. *Science* 265, 195–201.
- Peltier, W.R., 1996. Mantle viscosity and ice-age ice sheet topography. *Science* 273, 1359–1364.
- Reading, A.M., 2002. Antarctic seismicity and neotectonics. In: Gamble, J., Skinner, D., Henrys, S., Lynch, R. (Eds.), *Antarctica at the Close of a Millennium*, Proceedings of the 8th International Symposium on Antarctic Earth Sciences. R. Soc. N. Z. Bull. 35, 479–484.
- Ritzwoller, M., Shapiro, N., Levshin, A., Leahy, G., 2001. The structure of the crust and upper mantle beneath Antarctica and the surrounding oceans. *J. Geophys. Res.* 106 (B12), 30645–30670.
- Sabadini, R., Gasperini, P., 1989. Glacial isostasy and the interplay between upper and lower mantle lateral viscosity heterogeneities. *Geophys. Res. Lett.* 16 (5), 429–432.
- Stüding, M., Karner, G., Bell, R.E., Levin, V., Raymond, C., Tikku, A., 2003. Geophysical models for the tectonic framework of the Lake Vostok region, East Antarctica. *Earth Planet. Sci. Lett.* 216 (4), 663–677.

- Su, W., Dziewonski, A.M., 1991. Predominance of long-wavelength heterogeneity in the mantle. *Nature* 352, 121–126.
- Tackley, P.J., Stevenson, D.J., Glatzmaier, G.A., Schubert, G., 1993. Effect of an endothermic phase transition at 670 km depth in a spherical model of convection in the earth's mantle. *Nature* 361, 699–704.
- Tregoning, P., Twilley, B., Hendy, M., Zwart, D., 1999. Monitoring isostatic rebound in Antarctica using continuous remote GPS observations. *GPS Solutions* 2 (3), 70–75.
- Tregoning, P., Welsh, A., McQueen, H., Lambeck, K., 2000. The search for postglacial rebound near the Lambert Glacier, Antarctica. *Earth Planets Space* 52, 1037–1041.
- Trompert, J., 1998. Global seismic tomography: the inverse problem and beyond. *Inverse Problems* 14 (3), 371–385.
- Tsuboi, S., Kikuchi, M., Yamanaka, Y., Kanao, M., 2000. The March 25, 1998 Antarctic earthquake: great earthquake caused by postglacial rebound. *Earth Planets Space* 52, 133–136.
- Tushingham, A.M., Peltier, W.R., 1991. Ice-3G: a new global model of late Pleistocene deglaciation based upon geophysical predictions of post-glacial relative sea level change. *J. Geophys. Res.* 96, 4497–4523.
- Wahr, J.M., Davis, J.L., 2002. Geodetic constraints on glacial isostatic adjustment. In: Mitrovica, J.X., Vermeersen, L.L.A. (Eds.), *Ice Sheets, Sea Level and the Dynamic Earth*. AGU Geodyn. Ser. 29, Washington, pp. 3–32.
- Wessel, P., Smith, W.H.F., 1991. Free software helps map and display data. *EOS* 72, 441–446.
- Wessel, P., Smith, W.H.F., 1998. New, improved version of generic mapping tools released. *EOS* 79, 579.
- Wiens, D., Stein, S., 1983. Age-dependence of oceanic intraplate seismicity and implications for lithospheric evolution. *J. Geophys. Res.* 88, 6455–6468.
- Wu, P., 1992. Deformation of an incompressible viscoelastic flat earth with power-law creep: a finite element approach. *Geophys. J. Int.* 108, 35–51.
- Wu, P., 1992. Viscoelastic versus viscous deformation and the advection of pre-stress. *Geophys. J. Int.* 108, 136–142.
- Wu, P., Hasegawa, H.S., 1996. Induced stresses and fault potential in eastern Canada due to a disc load: a preliminary analysis. *Geophys. J. Int.* 125, 415–430.
- Wu, P., Johnston, P., 1998. Validity of using flat-earth finite element models in the study of postglacial rebound. In: Wu, P. (Ed.), *Dynamics of the Ice Age Earth: A Modern Perspective*. Trans. Tech. Pub., Zürich, Switzerland, pp. 191–202.
- Wu, P., Johnston, P., 2000. Can deglaciation trigger earthquakes in N-America?. *Geophys. Res. Lett.* 27 (9), 1323–1326.
- Wu, P., Johnston, P., Lambeck, K., 1999. Postglacial rebound and fault instability in Fennoscandia. *Geophys. J. Int.* 139, 657–670.
- Wu, P., Ni, Z., Kaufmann, G., 1998. Postglacial rebound with lateral heterogeneities: from 2D to 3D modeling. In: Wu, P. (Ed.), *Dynamics of the Ice Age Earth: A Modern Perspective*. Trans. Tech. Pub., Zürich, Switzerland, pp. 557–582.
- Wu, P., van der Wal, W., 2003. Postglacial sealevels on a spherical, self-gravitating viscoelastic earth: effects of lateral viscosity variations in the upper mantle on the inference of viscosity contrasts in the lower mantle. *Earth Planet. Sci. Lett.* 211, 57–68.
- Zwart, D., Tregoning, P., Lambeck, K., Johnston, P., Stone, J., 1999. Estimates of present-day glacial rebound in the Lambert Glacier region, Antarctica. *Geophys. Res. Lett.* 26 (10), 1461–1464.